The International Journal of Advanced Manufacturing Technology (2024) 134:369–387
https://doi.org/10.1007/s00170-024-14116-3

ORIGINAL ARTICLE

Understanding the machined material's behaviour in electro-discharge machining (EDM) using a multi-phase smoothed particle hydrodynamics (SPH) modelling

Ahmad W. Alshaer[1] · Ramy Abdallah[2] · Fatema H. Rajab[3] · Azeez A. Barzinjy[4,5] · Omonigho B. Otanocha[6]

Received: 20 March 2024 / Accepted: 8 July 2024 / Published online: 20 July 2024

Abstract

Electro-discharge machining (EDM) has been extensively employed for machining hard alloys, and its simulations have been widely conducted using finite element analysis (FEA). However, the majority of mesh-based models depended on forecasting the crater profile only based on the temperature gradient, without offering detailed data regarding the machined material properties. It is crucial to understand the behaviour of the machined material in order to accurately assess the flushing efficiency, analyse the wear on the electrode, and examine the interaction between the debris generated during machining and the remaining workpiece. This is done to ensure that no recast material is left behind after the EDM process. For the first time, a meshless smoothed particle hydrodynamics multi-phase model was implemented to gain practical insights and comprehensively understand a very intricate phenomenon that occurs within a very short time. Additionally, this approach is utilised to investigate the characteristics of the materials being machined. We utilised our SPH model to simulate both the capacitance- and transistor-based EDM of Ti–6Al–4V and AISI304 steel. Our simulation considered the temperature-dependent thermal properties and latent heats of the materials. The accuracy of our model was confirmed by comparing its results with experimental, analytical, and finite element analysis (FEA) results. The machined material was observed during its removal from the surface, and the dimensions of the resulting crater, as well as its aspect ratio and the rate at which the material was removed, were predicted with an error ranging from 2 to 22%. This error is far lower than that of the typical finite element (FE) prediction. This model lays the groundwork for a more complex model that will more accurately represent EDM and other similar manufacturing processes.

Keywords Electro-discharge machining · Simulation · Smoothed particle hydrodynamic · Debris · Material removal rate

✉ Ahmad W. Alshaer
awalshaer@uclan.ac.uk

Ramy Abdallah
r.m.a.m.abdallah@bham.ac.uk

Fatema H. Rajab
fatemarajab83@gmail.com

Azeez A. Barzinjy
azeez.azeez@soran.edu.iq

Omonigho B. Otanocha
otanocha.omonigho@fupre.edu.ng

[1] School of Engineering and Computing, University of Central Lancashire, Preston, UK

[2] School of Mechanical Engineering, University of Birmingham, Birmingham, UK

[3] Department of Laser and Optoelectronics Engineering, College of Engineering, Al-Nahrain University, Baghdad 1007, Iraq

[4] Scientific Research Center, Soran University, Kurdistan Region, Soran, Iraq

[5] Department of Physics Education, Faculty of Education, Tishk International University, Erbil, Iraq

[6] Department of Mechanical Engineering, Federal University of Petroleum Resources, Effurun, Warri, Delta State, Nigeria

1 Introduction

Electro-discharge machining has been used for decades in machining hard- and super-alloys due to their high hardness and limited machinability using conventional methods. Several works were conducted to study the process effectiveness on machining steels [1–4], titanium alloys [5–9], nickel alloys [10–13] and special aluminium alloys [14–16]. Over the last few decades, several simulations were developed in an attempt to understand the EDM process due to the complex physics that occur in a very short time [9, 17–19]. In this article, we will highlight the limitations of the existing models and propose a first-of-its-kind simulation to observe the behaviour of the machined material at practical and reasonable time and size scales.

1.1 Critical literature review

Yue and Yang [20] and Yang, Guo, Chen and Kunieda [21] developed a two-temperature molecular dynamics simulation approach to examine the mechanism of material removal in copper. Despite successfully simulating material removal and predicting temperature distribution, the model was only limited to a 2-D sub-microscale with a discharge time not exceeding 2000 ps. This model was significantly expensive to run due to the intricate atomic-level physics calculations involved, making it unfeasible or prohibitively costly to execute on a larger scale (micrometre scale) or to simulate multiple-spark machining.

Weingärtner, Kuster and Wegener [22] developed models for simulating wire electrical discharge machining (WEDM) of three distinct materials: AISI1010, CuZn39Pb3, and aluminium. The researchers considered the effects of latent heat of fusion and vaporisation during the WEDM process and investigated the impact of the heat source profile and the temperature-dependent material properties on the profile of the melting isotherm. Despite this claim, the authors did not provide the temperature-dependent properties they used in their work. The model demonstrates a strong concurrence with the experimental measurements of material removal rate (MRR). Although their trials yielded satisfactory results when accounting for latent heats, failing to provide the temperature-dependent properties for two materials within the published work hinders the replication of the study and limits its utility as a validation example.

The study conducted by Somashekhar, Panda, Mathew and Ramachandran [23] focused on the application of micro-electrical discharge machining (μ-EDM) in predicting the temperature distribution at the end of 200 μs for AISI 316. The researchers utilised an RC circuit and developed a MATLAB code for their analysis. The findings were solely verified by comparing them to another FEA model, without a discussion or prediction of the dimensions of the crater or Material Removal Rate (MRR). A similar study [24] constructed a similar model to evaluate the residual stresses resulting from μ-EDM of Ti–6AL–4V alloys and the aspect ratio was determined using an atomic force microscope and nano-indentation for a single spark protrusion. The results demonstrate exhibited significant disparities in the simulated crater's dimensions between simulations and the experiments, hence prompting inquiries regarding the reliability and precision of the projected material removal rate. In another study conducted by Qian, Yang, Wang, Lauwers and Reynaerts [25] on MRR during μ-EDM, the researchers observed oscillation of the sparking current and voltage when a high open-voltage was applied, and this phenomenon was predicted by electrical simulations and experimentally verified. In contrast to prevailing beliefs, the experiments showed that the negative current flow in a single sparking cycle also contributes to effective material removal on the workpiece. Cao et al. [26] studied the oscillation wave analysis and incorporated the randomisation of spark machining locations in μ-EDM high aspect ratio drilling using three-phase flow. Their work focused on the impact of bubble generation and debris on the flushing efficiency.

Focusing on the surface topography, Izquierdo, Sánchez, Plaza, Pombo and Ortega [27] run a 3-D FEA simulation to estimate the surface roughness on an EDM machine surface of AISI D2 tool steel using repeated sparks. Their model studied the influence of the probability of occurrence of a single or multiple sparks and the gap size between the electrode and the workpiece on R_a value during machining. Due to the stochastic nature of the process, the analysis in this study only focused on the overall effect of the multiple pulses on surface roughness, neglecting the verification of individual protrusion diameters which is noted in the large variation in the material removed per discharge. Their work was followed by Jithin, Bhandarkar and Joshi [28] who developed a simpler 2-D MATLAB numerical model to predict the surface roughness in multi-spark EDM without the need for FEA. The model prediction accuracy was around 11.5% in estimating the R_a value during EDM of Ti–6Al–4 V alloy but only showed a 2-D section. Moreover, both models were more accurate for short pulse-ON time (<200 μs), than long pulse-ON time (>200 μs) for which the error exceeded 100% in a few cases.

Yeo, Kurina and Tan [29] conducted a comparative analysis of five distinct electro-thermal models to simulate the EDM of AISI 4140 Steel. These models included Snoeys's model [30], Van Dijck's model [31], Beck's model [32, 33], Jilani's model [34–36], and DiBitonto's model [37]. The

primary aim of the research was to investigate the impact of heat source and process factors on the temperature gradient, geometry of the crater, and MRR at the cathode. The study's findings indicate that DiBitonto's model is regarded as the most suitable for providing an accurate estimation of the machining particularly when dealing with high discharge energy.

Bhaumik and Maity [38] predicted MRR and temperature distribution during the machining of Ti-5Al-2.5Sn alloy. However, FE elements were deleted from the domain when their temperature was over the melting point, assuming that the dielectric liquid would flush away the molten metal. Despite finding this assumption is true by Cao et al. [26] who studied high aspect ratio drilling, Bhaumik and Maity [38] did not provide a citation or evidence of that assumption at the time of conducting their work. Furthermore, a fixed spark radius was presumed based on the process parameter, and the plasma flashing efficiency was considered constant, disregarding its dependence on the current and the pulse-ON time. The same strategy was used by Assarzadeh and Ghoreishi [39] to predict the crater's dimensions and MRR in AISI 304 using Abacus. Kalajahi, Ahmadi and Bavil Oliaei [40] utilised surface response analysis to forecast the impact of different parameters on the MRR during machining of AISI H13 tool steel. However, no information was provided regarding the dimensions of the crater removed by a single spark.

It is pertinent to note that the accuracy of the simulations of EDM relies on the correct selection of the plasma flushing efficiency, energy fraction value, and the radius of the plasma as they significantly affect the results. Several studies [18, 41–43] investigated the extension of the previous factors' effect on the process modelling and provided a detailed insight into this matter. Gholipoor et al. [41] provided an analytical solution to predict the variable plasma channel radius with time, while Padhi et al. [44] studied the effect of the plasma flushing efficiency on a single discharge machining of steel and Kliuev et al. [45] related the energy absorption fraction to the experimental results for a better accurate numerical prediction of the crater's dimensions.

It can be seen from the literature that finite elements models can only be useful to predict the overall crater's dimensions. However, their limitations are evident because they appear to have limited effectiveness in yielding data regarding the removed material (including its velocity, temperature and ejection direction), observing the machined material's redeposition on the cathode/anode, the electrodes wear, or observing the flushing efficiency using multiphase simulations. Moreover, most of the finite element models were based on a fixed plasma/spark radius while it is, in reality, variable with time as the plasma channel grows. Furthermore, many of the FE models rely on removing elements with temperatures higher than the melting point without consideration of the material's vaporisation effect.

In this article, the first-of-its-kind smoothed particle hydrodynamics (SPH) model is developed to overcome the limitations of FE modelling and to fully observe and analyse the machined material's behaviour to better understand its effect on the flushing efficiency, tool wear and recast during EDM. The SPH model was validated against a large number of published experimental and FEA works.

2 Model description

2.1 Materials properties

Our SPH model was validated using two different alloys, namely Ti–6Al–4V and AISI 304, and machines with two types of EDM pulse generators including resistor–capacitor (RC circuit) and transistorised generators. Figures 1, 2 and 3 show the variation of the thermo-physical properties of the alloys with temperature.

2.2 Physical phenomena

2.2.1 Heat transfer governing equations

The mechanism of material removal in EDM of metallic alloys is mainly based on thermal vaporisation due to the increase of the workpiece temperature to the boiling point in a significantly short time. Figure 4 shows a schematic of a typical EDM process.

Depending on the dielectric fluid and the workpiece materials, part of the thermal energy is wasted in the dielectric fluid and a portion of the energy is absorbed by the workpiece. The portion of the energy absorbed by the workpiece is called plasma flushing efficiency (PFE) and various values

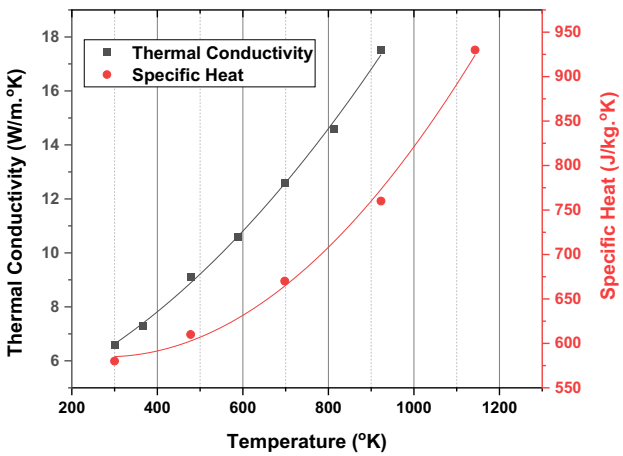

Fig. 1 Temperature-dependent thermal properties Ti–6Al–4V alloy [24]

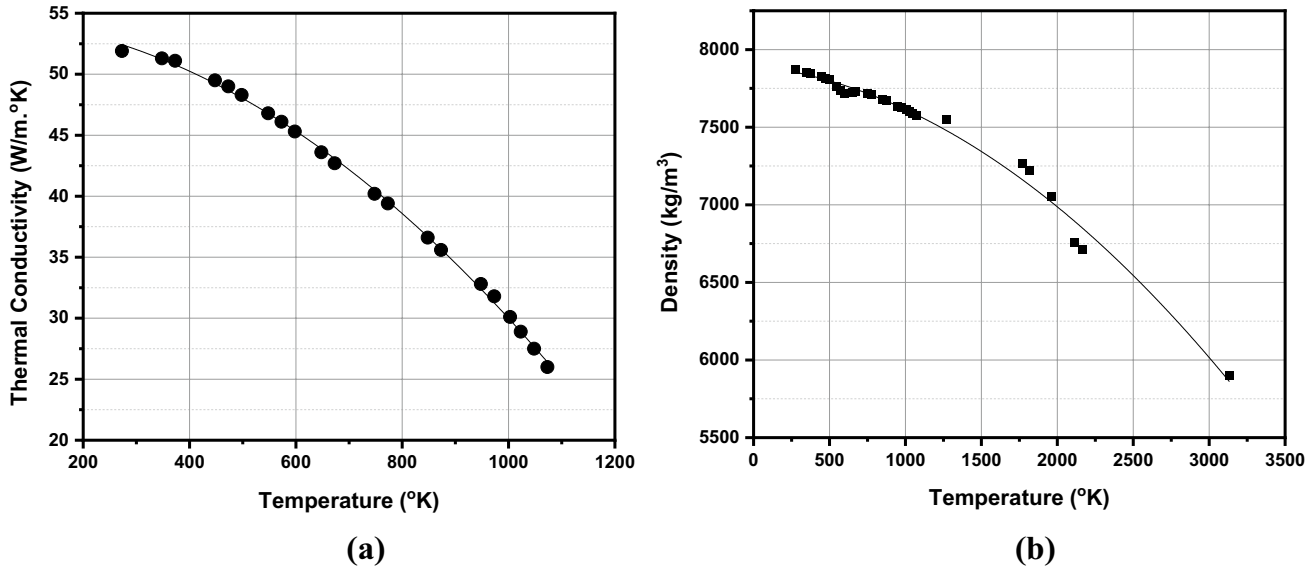

Fig. 2 **a** Thermal conductivity and **b** density variation with temperature of AISI 304 alloy [39]

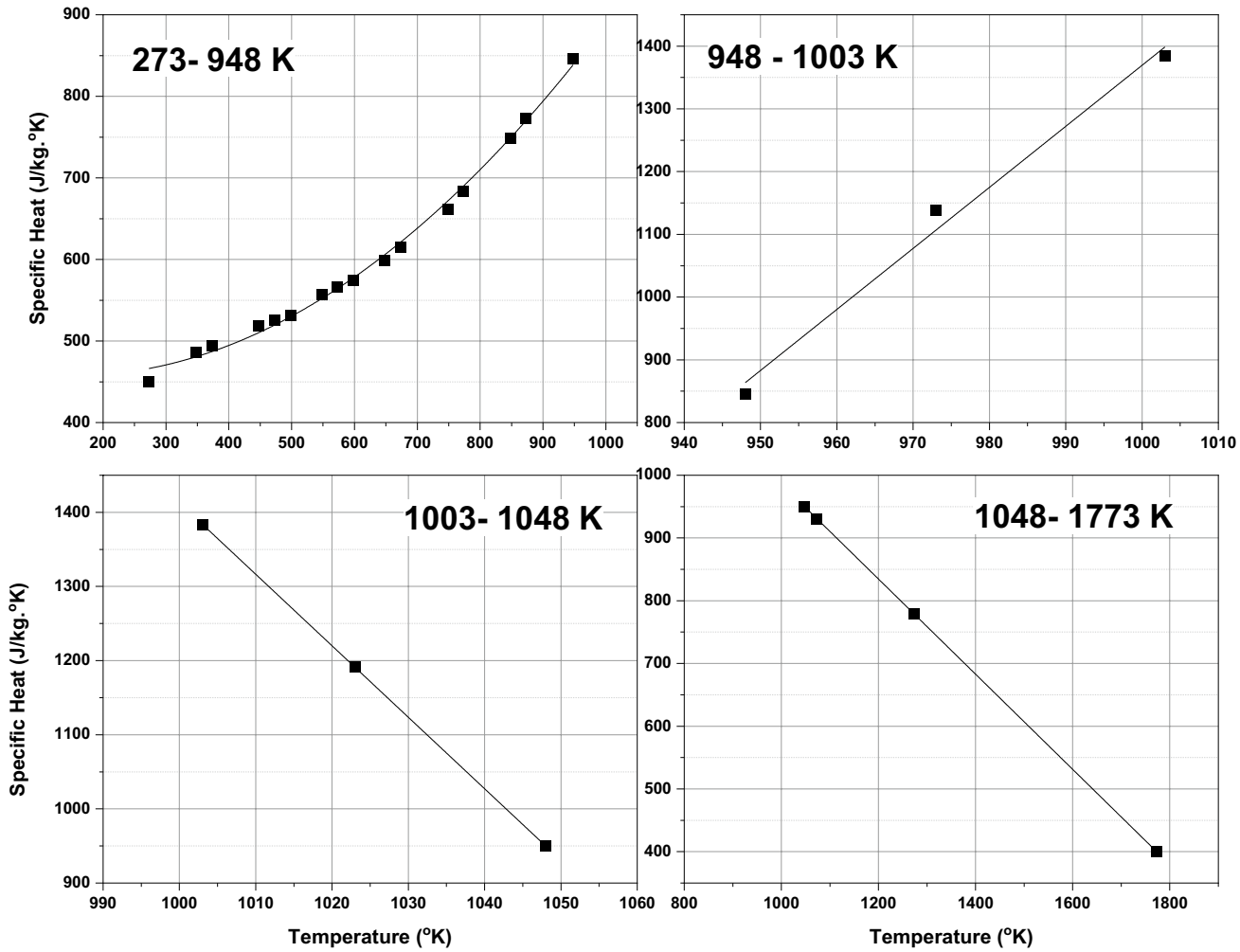

Fig. 3 Temperature-dependent specific Heat of AISI 304 alloy for a different range of temperature [39]

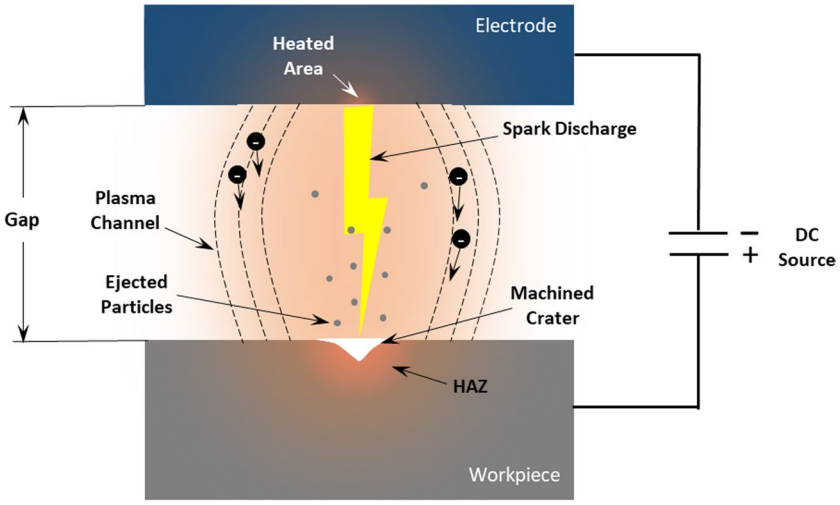

Fig. 4 Simplified schematic EDM machining using a single spark

were considered in this paper depending on the experiments or the reference simulations parameters.

The differential equation of heat transfer can be stated analytically and with consideration for the external heat sources as follows [46]:

$$\rho\, c_p \frac{dT_i}{dt} = \nabla(k\nabla T) + Q - Q_v \tag{1}$$

where k (W/m.K) thermal conductivity, T (°K) temperature, Q (W/m^2) the heat source, and Q_v heat loss due to convection.

The heat loss Q_v can be formulated using [46]:

$$Q_v = h_c\left(T_s - T_0\right) + \varepsilon\sigma\left(T_s^4 - T_0^4\right) \tag{2}$$

where h_c (W/m^{2}K) convection factor, ε the emissivity, $\sigma = 5.67 \times 10^{-8}$ (W/m^{2}K^4) the Stefan-Boltzmann constant, T_s and T_0 are the surface and the initial temperatures, respectively. Depending on the validation case tested, the values of the coefficients and factors would be different and heat loss due to emission was not always considered.

The model has been validated using both (capacitance-based) and (transistor-based) EDM mechanisms. Figure 5 shows the different electrical circuits used in common EDM machines.

The discharge energy deposited on the surface of the workpiece is calculated in the relaxation circuit by [24]:

$$E_d = \frac{C.V^2}{2} \tag{3}$$

where E_d (J) is heat quantity, V (V) the voltage and C (F) capacitance.

While E_d is given for a transistorised generator by [47]:

$$E_d = V\ .I.\ t_{ON} \tag{4}$$

where I (A) is the discharge current.

By considering the various process-related factors including the pulse-ON-time and flushing efficiency, the Gaussian heat distribution can be expressed as:

$$Q = \frac{E_d.F_c.\eta}{\pi.r_s^2.t_{ON}} \exp\left[-\alpha\left(\frac{r}{r_s}\right)^2\right] \tag{5}$$

where Q heat quantity (W/m^2); r_s (m) plasma channel radius; t_{ON} (s) spark-ON-time; r is the distance from the centre of

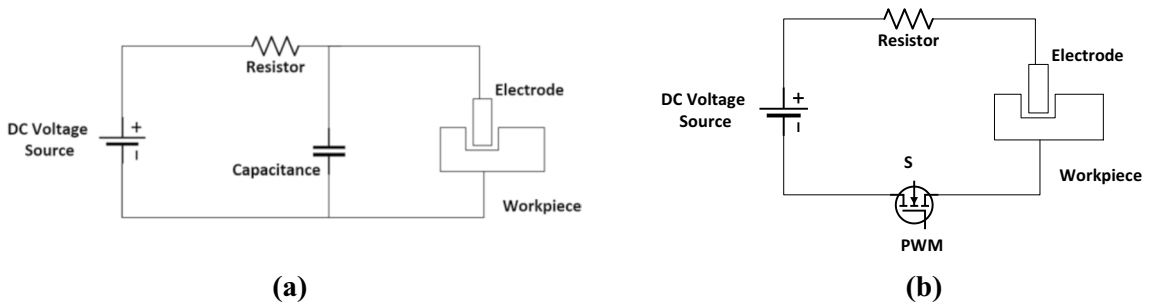

Fig. 5 Discharging pulse generator in EDM. **a** Resistor–capacitor and **b** transistorised circuits

the plasma channel; η plasma flushing efficiency; F_c cathode energy fraction, which is the fraction of heat absorbed by the workpiece; and α a constant different in each research work.

2.2.2 Plasma channel radius

The plasma channel radius (m) used in [39] is given as:

$$r_s = 2040 \times 10^{-6}.\, I^{0.43}.t_{ON}^{0.44} \tag{6}$$

While a different expression that only relies on the pulse-ON time was used in [24]:

$$r_s = k\,.\,t_{ON}^{3/4} \tag{7}$$

where k is constant.

It should be noted that Eq. (7) was used by Murali and Yeo [24] to determine the crater's radius, by making it equal to the plasma channel radius. This is not, of course, what occurs in real life and the practicality of this assumption is discussed in the "Results" section.

Moreover, the plasma channel radius was taken constant in most of the previous works, while in our SPH model, the value was changed dynamically as the simulation developed. Hence the ultimate value of the plasma channel radius was dependent on pulse-ON time and the current, but its value was growing with time until it reached the largest value at the end of the discharge pulse. This mechanism more precisely simulates the physical phenomena and hence offers a more accurate simulation of the crater's dimensions.

It is crucial to acknowledge that at the start of the simulation, when time is zero, the channel radius will also be zero. This leads to a singularity of the heat source at the surface, which ultimately causes the simulation to report an error. Hence, it is necessary to set a small, yet non-zero value to r_s at the beginning of the simulation, which subsequently increases with time until it reaches its maximum value during the discharge phase. This value is taken as the radius calculated at (0.1–0.5 µs) until this time is reached and the radius equation is then applied. This range is quoted depending on the discharge energy level that may produce unphysically high energy density at 0.1 µs time compared to 0.5 µs, which is still a very small time compared to the scale of the pulse-On time that can reach hundreds of micro-seconds. This may not be the case for some of the validation cases in this article, where the published works quoted a constant radius during the entire simulation.

2.2.3 Plasma flushing efficiency (PFE) and energy fraction (F_c)

During EDM, part of the discharge energy is wasted to the dielectric and the tool, while only a small portion is absorbed by the workpiece and used in machining. This small portion is usually described by the cathode energy fraction (F_c) that defines the amount of the useful energy taken as a ratio from the total heat flux generated by the plasma. It must be said that this ratio is dependent on several factors such as tool, workpiece and dielectric's thermal properties, flushing phenomena, machining gap, polarity and discharge parameters [48–50]. Therefore, it is extremely challenging to define a universal value for F_c and different published literatures use different values ranging from 8 to 50% [28, 39, 47, 51].

Additionally, the percentage of the energy absorbed by the workpiece is not fully utilised in the machining process since a percentage of it is wasted due to conduction, latent heating, convection and radiation at the surface. Hence another ratio is introduced to account for this waste, namely the plasma flushing efficiency (PFE). This term is the ratio between the actual machined amount of the materials compared to the theoretical amount removed by a single spark if all the energy is used in machining. PFE is also dependent on the process parameters and the material properties of both the tool and workpiece. Many research works assume 100% PFE [8, 24, 38, 39], while others use either a constant value or a dependent value on the discharge current and the pulse-ON-time [28, 47].

In our model, we used a variable PFE depending on the validation case; however, a variable flushing efficiency is recommended since experiments showed that for lower pulse energies, the PFE decreases and a larger discrepancy is observed between the simulations and experiments, compared to the higher energy sparks [52].

2.2.4 Vapour pressure

Depending on the surface temperature, the Clausius–Clapeyron equation can be used to compute the vapour pressure created by the discharge ionisation of metal [53]:

$$P_{\text{vap}} = P_{\text{atm}} \exp\left(\frac{L_v}{R}\left(\frac{T_s - T_b}{T_s.T_b}\right)\right) \tag{8}$$

where P_{atm}, R, L_v, T_s and T_b are the atmospheric pressure, gas constant, latent heat of vaporisation, surface temperature and the boiling temperature respectively.

2.2.5 Vapour velocity

The vapour velocity can be approximated by using the average velocity in the normal direction at temperature T_s under the assumption that the vapour particles are ejected off the surface with a one-dimensional Maxwellian velocity [54]:

$$v_{\text{vap},s} = \sqrt{\frac{2\,k_B\,T_s}{\pi\,m}} \tag{9}$$

where k_B is Boltzmann constant (1.38×10^{-23} m^2 kg/s^2 K), and m is the atomic mass.

3 SPH methodology

3.1 SPH interpolation

In SPH, The computational domain is partitioned into randomly dispersed particles, each of which has a different mass m_i, volume ω_i, pressure P_i, and velocity v_i [55]. A local interpolation for a group of surrounding particles, at a certain time step, can be used to determine the value of a function $A(r)$ at location r. The interpolated value of the function can be obtained in its continuous form [56]:

$$\langle A(\boldsymbol{r})\rangle = \int_{\Omega} W(\boldsymbol{r}-\boldsymbol{r'},h)A(\boldsymbol{r'})d\Omega \tag{10}$$

where r is a position vector, $<>$ denotes approximation, W is a weighting function called the smoothing kernel, h is the smoothing length (a characteristic length scale of the kernel). The smoothing kernel for the interaction between two SPH particles, i and j, can be expressed conventionally as follows [57]:

$$W_{ij} = W(\boldsymbol{r}_{ij},h) = \frac{1}{h^n} f\left(\frac{\left|\boldsymbol{r}_i-\boldsymbol{r}_j\right|}{h}\right) \tag{11}$$

where n is the number of spatial dimensions, f is a function of h and $r_{ij}=|r_i—r_j|$ the distance between two particles i and j.

The discrete SPH form of the function $A(\boldsymbol{r})$ is as follows:

$$\langle A_i(\boldsymbol{r})\rangle = \sum_j m_j \frac{A_j}{\rho_j} W_{ij} \tag{12}$$

where ρ_j and m_j are the particles density and mass respectively.

The gradient of the considered function can be calculated by taking the kernel gradient into account in the approximation:

$$\langle \nabla A_i(\boldsymbol{r})\rangle = \sum_j m_j \frac{A_j - A_i}{\rho_j} \nabla_i W_{ij} \tag{13}$$

A smoothing kernel can be Gaussian, quadratic, cubic (B-spline), or higher order (fourth and fifth order) kernels. Since the cubic spline is widely used in SPH and can be used to approximate the Gaussian function, it was determined to be the basis for our model. The following equation can be used to represent the cubic spline [56]:

$$W(r_{ij},h) = \alpha_D \begin{cases} 1-\frac{3}{2}q^2+\frac{3}{4}q^3 & 0\le q\le 1 \\ \frac{1}{4}(2-q)^3 & 1\le q\le 2 \\ 0 & 2\ge q \end{cases} \tag{14}$$

where $q = r_{ij}/h$, α_D is a normalization parameter to ensure the unity integral of the kernel, with a value of $7/4\pi h^2$ for 2-D domain. Figure 6 shows particle i and its neighbour particle j within a smoothing kernel of a radius 2 h.

The temperature gradient is calculated using the heat source at the workpiece surface and particles with temperature exceeding the material's boiling point are ejected from the surface, forming a crater. The effect of the plasma flushing efficiency, latent heat quantities, and the temperature-dependent properties were considered in our SPH model. Moreover, the influence of the particles movement and the associated convection is captured by default due to the Lagrangian nature of SPH.

3.2 Model assumptions

The SPH model is used to simulate an individual spark taking into consideration temperature dependence thermophysical properties of the workpiece material, a Gaussian heat flux, variable plasma channel radius, plasma flashing efficiency, and the latent heat of fusion and vaporisation. Our unique model can show the thermal history in the workpiece during a single spark heating and give full information about the dynamics of the machined debris in terms of pressure and velocity. This single-spark model can be easily extended to simulate multiple stochastic sparks that occur during EDM.

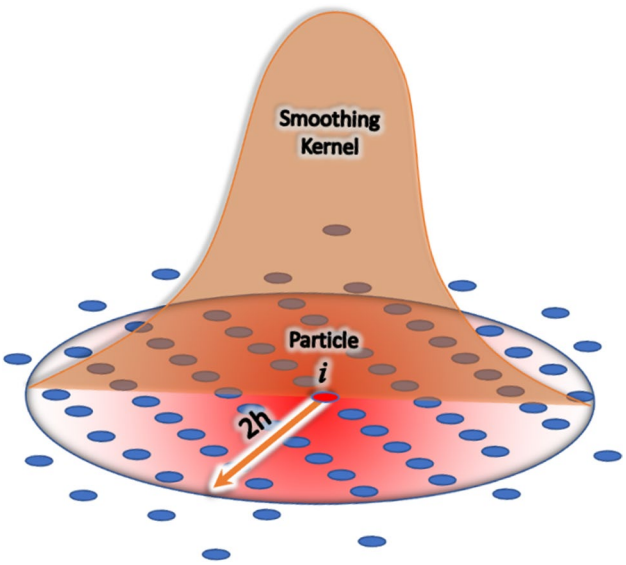

Fig. 6 Particles i and j within the smoothing kernel support

The following assumptions are made for the sake of simplicity:

1. The thermophysical properties of the workpiece materials are temperature-dependent.
2. The plasma channel radius is dependent on the pulse-on time and the current in the transistor-based EDM. To avoid singularity at the beginning of the simulation due to the "zero" value of the radius, a very small radius of the plasma channel is used. Further information is provided in Section 2.2.2.
3. A Gaussian heat flux distribution is used and is applied to the surface of the workpiece
4. The dielectric fluid affects the plasma flashing efficiency (PFE), the fraction of heat (F_c) absorbed by the workpiece, and the convective coefficient h_c. The value of these parameters is computed to suit the assumption in the validation cases and experiments.
5. The electrode wear is not simulated.
6. The heating of the ejected particles stops when they leave the surface.

The parameters used in the SPH model are given in Table 1.

Table 1 Modelling parameters used in the smoothed particle hydrodynamics simulations

Variable	Value
Particle spacing (Δx)	200–500 nm (depending on the case)
h	$1.5\Delta x$
Timestep (dt)	1.0 ns
Time-stepping algorithm	Predictor–corrector
Density filter	Shepperd filter
CFL number	0.1
Simulation physical time	At least 1.5 × pulse-ON time

4 Results and discussion

4.1 Resistor–capacitor (RC) circuit

Our model was validated against the data in [24] using Ti–6Al–4V alloy as the workpiece's materials and using the process parameters given in Table 2. A convergence study was carried out and the largest particle spacing was found to be 0.2 µm, which is way smaller than any mesh resolution found in the literature used in the validation of our model.

Figure 7 depicts the different stages of the machining of Ti–6Al–4V alloy over a period of 100 ns and the formation of the final protrusion. It is shown that the material is being removed layer by layer and plasma heats up the next layer until the spark-ON-time is over, offering a more realistic behaviour compared to the FE approach which virtually removes the "molten" elements after the pulse-ON time has passed.

It is pertinent to mention that the molten material is pushed to the sides of the crater due to the Marangoni effect and some particles do not have adequate time to leave the molten area and hence convection takes place and moves them to the edges of the crater, a behaviour confirmed by other researchers [58]. The edges cool down directly after the pulse finishes and forms a ring around the crater. The temperature at 1 ns reaches high values above 6000 °K, which is higher than the boiling point of the alloy.

Figures 8 and 9 provide a comparison of the crater profile and the material removal rate between te SPH model and the experiments by Murali and Yeo [24]. It can be clearly seen from Fig. 8 that the crater dimensions produced using SPH modelling, and experiments are in good correlation with less than 0.4 µm difference in the width. Although the crater predicted using SPH is wider at the bottom compared to the cone-like crater shown using the atomic force microscope (AFM), the error in the material removal rate was less than 20%, as shown in Fig. 9. This can be explained by the variable intensity of the actual plasma channel, which starts at a very high energy intensity at its centre and then expands and reduces in intensity

Table 2 Simulation parameters used in RC-based EDM used in our SPH model and [24]

Variable	Value	Variable	Value
Workpiece material	Ti–6Al–4V	Room temperature	300 K
Spark radius	2.1 µm	Melting temperature	1571 K
Spark ON-time	100 ns	Boiling temperature	2367 K
Capacitance	3000 pF	Density	4400 kg/m^3
Discharge voltage	110 V	Thermal expansion	8.6×10^{-6} 1/K
Particle spacing (Δx)	0.2 µm	Cathode energy fraction (F_c)	0.08 [24]
SPH domain dimensions	20 µm × 10 µm	α	3
Total number of particles	6555	PFE	100%
Time step	200 ps		

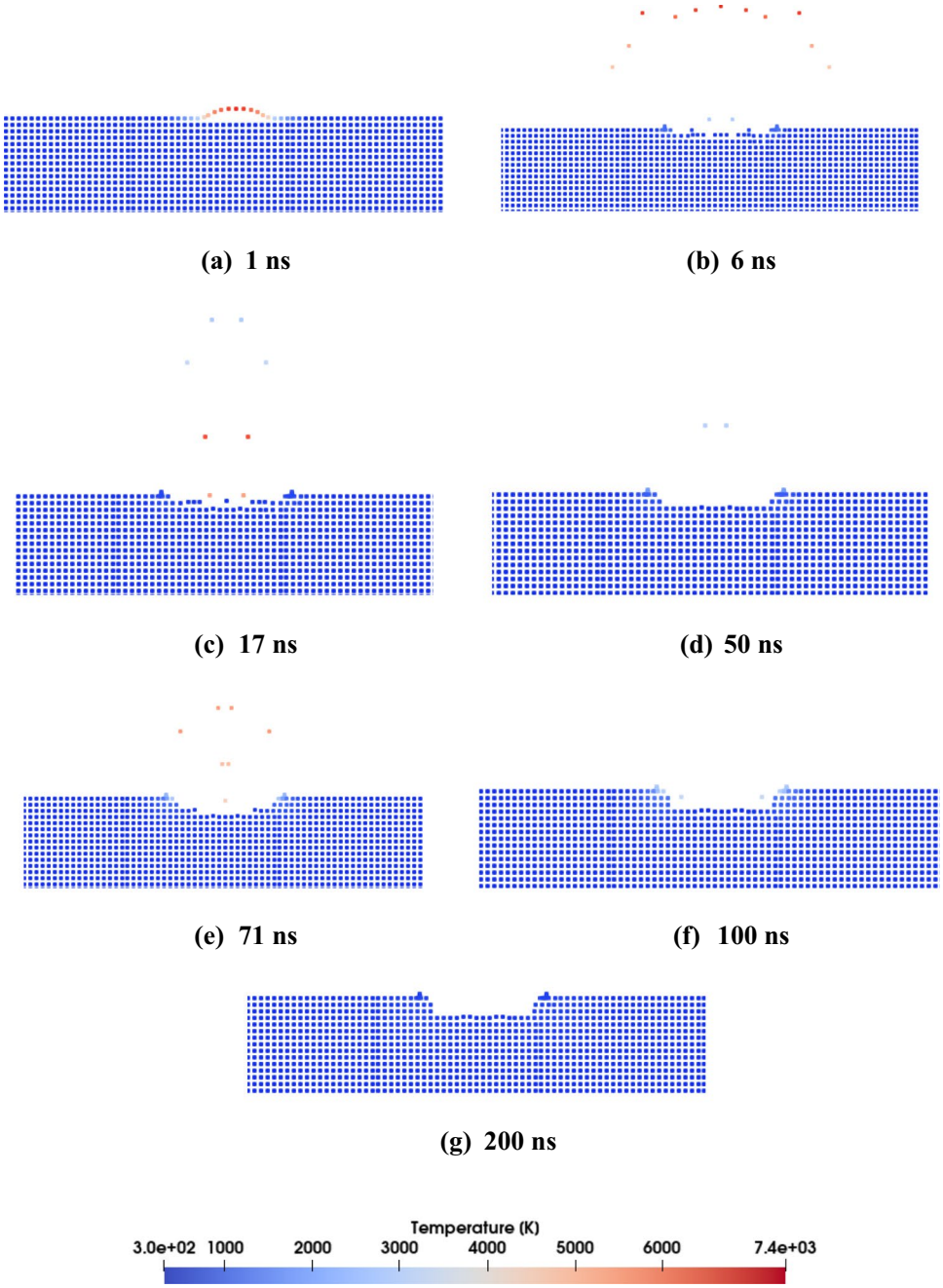

Fig. 7 Temperature distribution and crater profile in Ti–6Al–4V workpiece using a single 100-ns pulse

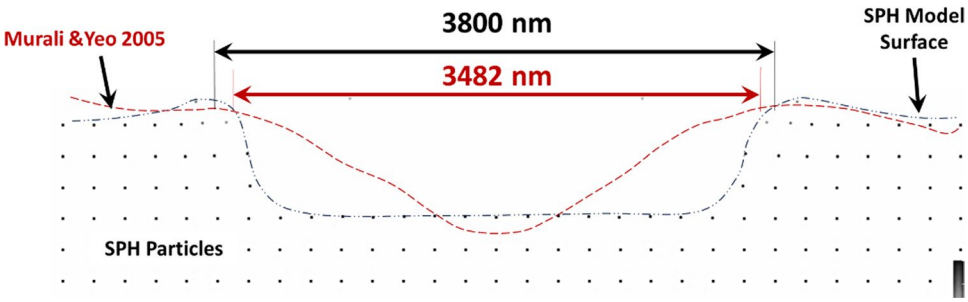

Fig. 8 A comparison of the crater profile at the end of the 100-ns pulse-ON time between SPH (centreline) and experimental results (dashed line) by Murali and Yeo [24]

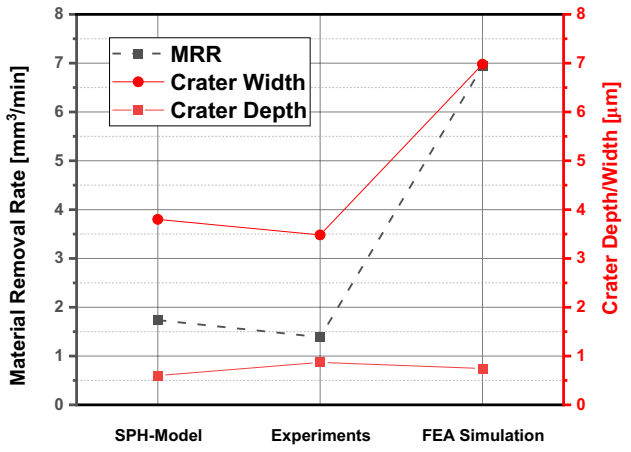

Fig. 9 Comparison of **a** the material removal rate and **b** crater dimensions between SPH model and experiment by Murali and Yeo [24]

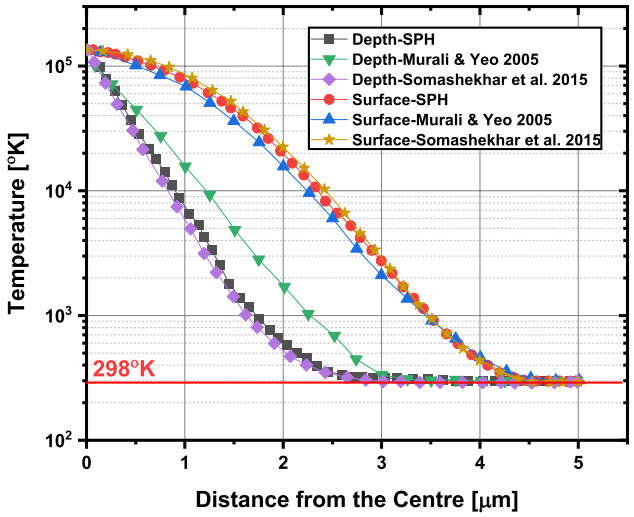

Fig. 10 Temperature gradient along the surface and depth from the spark centre against [24] and [23]

with time until it vanishes at the end of the pulse-ON-time. This concentrates the energy at the centre at the beginning of the pulse and leaves a cone-line shape crater compared to the constant cylindrical plasma channel assumed in the simulations, which leads to wider surface heating and creates a trapezoid-like crater. The selection of the constant plasma channel radius was intended to create a comparable simulation environment to that adopted in the FEA.

In addition, the SPH model assumes a uniform and homogenous surface without defects such as non-uniformities, coatings or imperfections that may lead to non-uniform or unsymmetrical machining, even when a Gaussian heating source is assumed.

It can also be noted that our SPH model produces a more comparable result to the AFM measurements than the FEA developed by the same researchers [24]. The FEA produced a crater with 3164 µm and 1835 µm in radius and depth respectively although those numbers are two times larger than the AFM measurements. Therefore, Murali and Yeo [24] only compared the aspect ratio for the crater and justified the considerable difference in dimensions by only removing the "molten" material without showing the results for removing the vaporised material, which was done in our more realistic model. A full comparison of the crater dimensions is provided in Fig. 9.

Figure 10 compares the temperature distribution along the depth and surface of the Ti-6AL-4V samples between SPH results and FEA simulations run by Murali and Yeo [24] and Somashekhar, Panda, Mathew and Ramachandran [23]. SPH results correlate very well with both FEA simulation results along the workpiece surface and depth and prove that the SPH model offers a credible prediction for both the temperature field and the final crater's dimensions. This comparison was carried out at 100 ns time after heating the material with a single pulse without removing the material, following the same procedure presented in the references mentioned earlier.

It is clear that the temperature significantly drops by an order of magnitude within only 1 µm depth, indicating that the conduction does not have adequate time to dissipate heat, compared to the discharge plasma heating that is concentrated on the surface.

The good agreement among all models is evident along the surface although a considerable difference can be traced across the depth in Murali and Yeo's FEA model, which produces significantly higher values. The temperature at the surface in their model, however, somehow matches the values from other models and the difference may be related to the poor mesh resolution along the depth in their model, since no convergence study was presented in their work.

Using the same material, the SPH model was also validated against Chen et al. [8] simulation, which studied the crater's dimensions using various capacitance values.

It can be seen from Fig. 11 that despite creating smaller craters, the SPH model produced comparable results to the numerical and measured crater's dimensions. The difference can be related to the different eroding environments created between the experiments and the simulations that assume a constant energy fraction and discharge energy source, something different to the real-life scenario in which the energy peaks at the beginning of the discharging process (due to full capacitance charge) and reduces at later stages [8]. Moreover, SPH particles that leave the surface require some time to be distant from the surface to allow the detection of the new surface particles that would be heated by the spark and the simulation carries on. This time may have caused some delay in heating of the underlying layers and hence produced slightly smaller craters. Additionally, Chen et al.'s. model

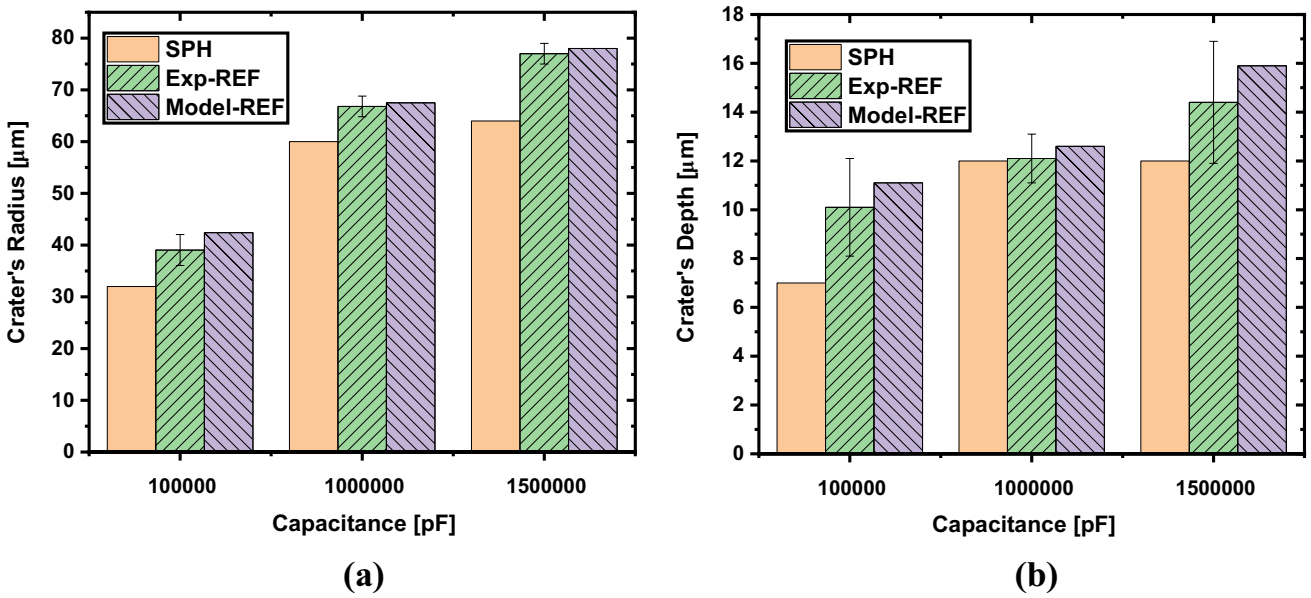

Fig. 11 Effect of process parameters on crater **a** radius and **b** depth compared to experimental and FEA results ($V = 220$ V, $t_{ON} = 5$ µs) [8]

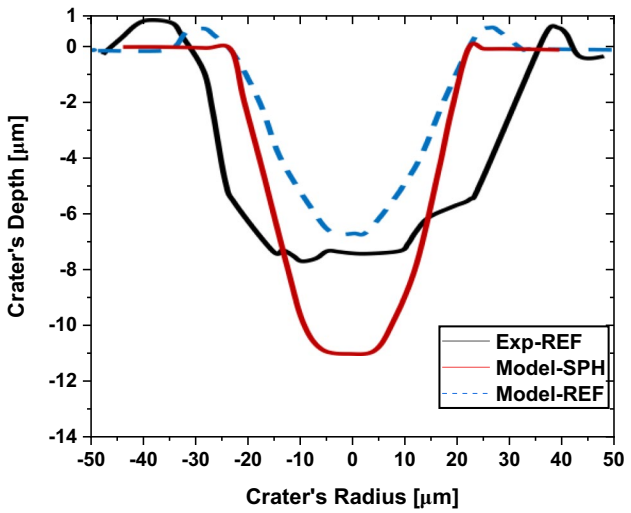

Fig. 12 Effect of process parameters on crater's dimensions compared to experiments and simulation (please note the different scales for the axes) [59]

overpredicted the dimensions due to the consideration of the plasma recoil pressure that would push the molten materials against the workpiece and produce larger craters, which is not considered in our current SPH model.

Another case (Fig. 12) was run against Singh et al. [59] who studied the effect of the plasma channel pressure on modelling EDM of Ti–6AL–4V alloy using RC circuits. The results showed that the assumed plasma pressure has a significant impact on the crater's profile under the same process parameters. For a comparison to the experiments, 2 MPa plasma pressure was selected to predict the shallowest crater [59]. Both FE and SPH models predicted the same crater width (around 25 µm) but the difference in the depth was greater (around 35%). This may be related to the resolidification phenomena that are not considered in the current SPH model, which assumes that once the material leaves the surface, it gets flushed by the dielectric fluid. This opens the possibilities for further improvement of the current model.

Although the Singh et al. model predicts closer depth to the experiments, it creates a much smaller profile when combined with the underestimated crater's width. However, the SPH model offers a better agreement in the overall material removal rate because it predicts a more accurate crater's volume with MRR of 0.148 g/min (SPH) against 0.163 g/min (experiment), compared to 0.069 g/min predicted by the FEA.

4.2 Transistorised pulse-generator circuit

The most prevalent kind of EDM in the market utilises transistors to accurately regulate the discharge current and pulse temporal features. This effectively addresses the issues of recharging delay, limited control over spark ON/OFF periods, and energy consumption that are typically observed in RC systems. Our SPH model was also tested using this type of discharging circuit, and the findings were then compared to published experiments, two finite element simulations, and an analytical solution for machining AISI 304 Steel. The process parameters used in the SPH model are provided in Table 3.

Table 3 Simulation parameters used in transistor-based EDM used in our SPH model [39]

Variable	Value	Variable	Value
Workpiece material	AISI 304 steel	Latent heat for melting	247 kJ/kg
Discharge voltage	20 V	Melting temperature	1808 K
Discharge current	40, 50, 60 A	Boiling temperature	3100 K
Pulse-ON-time	22, 125, 200 µs	Density	7872 kg/m^3
SPH domain dimensions	200 µm × 500 µm	Thermal expansion	7.3×10^{-6} 1/K
Particle spacing (Δx)	5 µm	Energy fraction (F_c)	0.18 [39]
Time step	1 ns	α	4.5
Total number of particles	19,075	Convection coefficient	688.9–836.2 W/(m^{2}K)
Plasma flushing efficiency	100% in [39] (only used in validation against Assarzadeh et al. 2017) $0.1093 + 2.238\times10^{-2}I - 8.441\times10^{-4}t_{on} - 4.67\times10^{-5}I.t_{on} + 4.912\times10^{-6}t_{on}^2$ in [47] (only used in validation against Jithin et al. 2018)		

Figures 13, 14, and 15 depict the progression of micromachining on a workpiece under various process settings, as outlined in Table 3, and illustrate the velocity vector field. As anticipated, increasing the discharge pulse energy results in higher velocities and temperatures of the ejected particles, which in turn leads to accelerated machining and a greater crater volume. Particles at the beginning exit the top surface in a direction perpendicular to it, although with varying magnitudes of velocity. Consequently, during the initial stages of machining, the first group of particles move upwards and align in an arc shape due to the highest velocity observed at the centre, while the following particles located on the sides of the crater exit at an angle determined by their surface normal vector. Particles following the disappearance of the plasma channel exhibit reduced velocity as a result of their temperature having already lowered due to conduction and convection and are ejected in random directions, depending on where the belong on the surface.

Furthermore, it is evident that the crater profile is non-uniform in all instances, since certain particles are propelled towards the edges of the crater as a result of the Marangoni effect, also known as thermal convection. The particles are unable to leave the surface because their temperature decreases through conduction, causing them to stick to the upper edges of the crater. This phenomenon resembles the movement and transfer of materials to the sides, which is commonly observed in micromachining, ablation, welding, and similar processes.

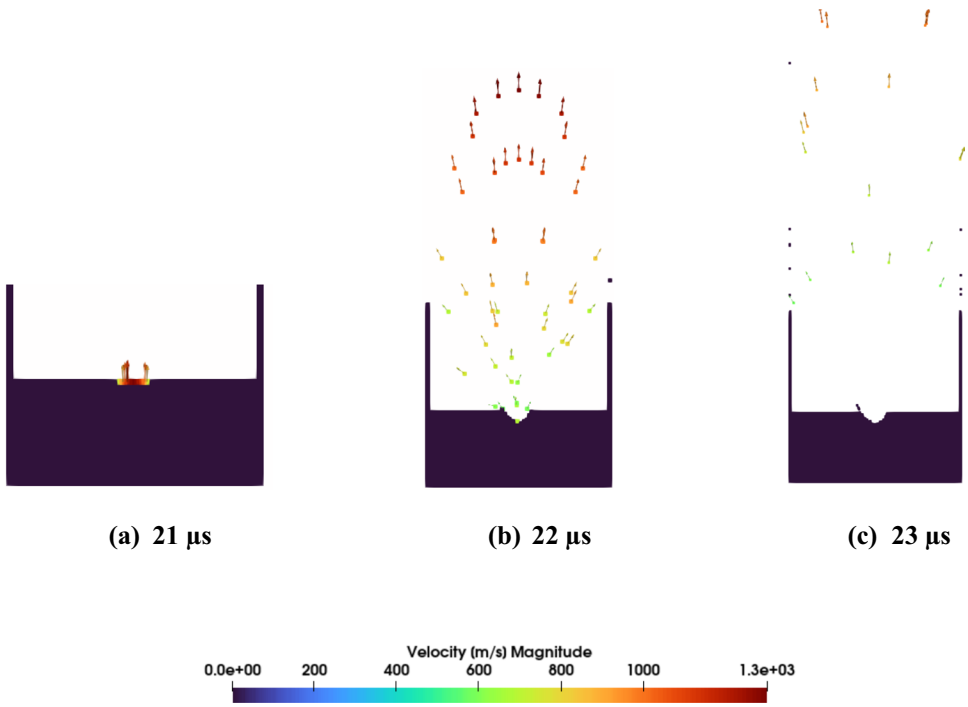

Fig. 13 Machined material velocity field and the crater formed using 40 A and 22 µs spark

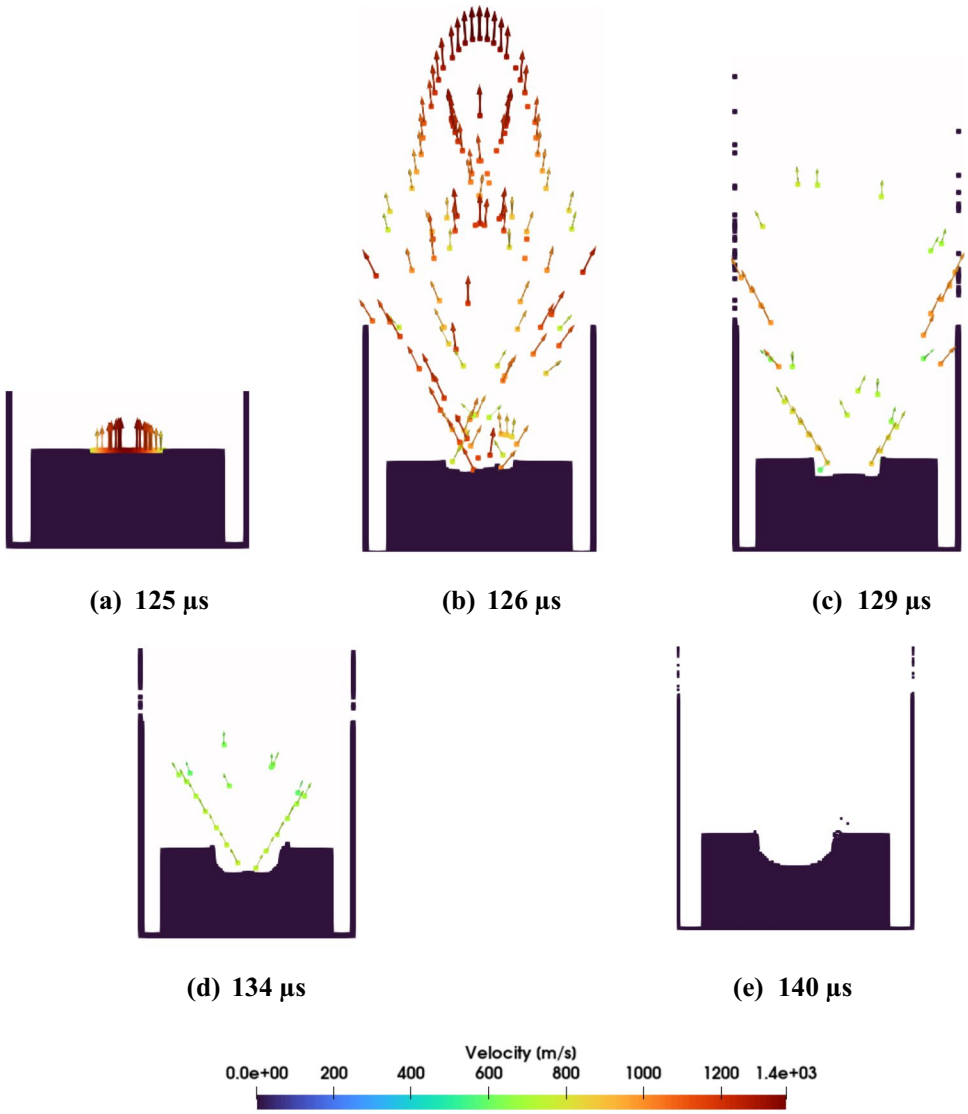

Fig. 14 Machined material velocity field and the crater formed using 50 A and 125 µs spark

Upon reaching the boundaries of the domain, the moving particles cease their momentum and come to a halt, hence discontinuing any further interaction with other particles.

To analyse the results from Figs. 13, 14, and 15, a comparison is provided in Fig. 16 regarding the crater profiles created by SPH simulations, FEA and the experimental data in the literature. In the same figure, the temperature gradient is depicted, and the heat-affected zone can be easily identified, while the ejected material can only be visualised using the SPH model. It is important to note that the particle spacing remains consistent throughout all instances, but the spacing may seem larger in Fig. 16a due to magnifying the machine area.

Table 4 gives the exact values for the crater depth and width for the three cases while Fig. 17 gives a graphical representation of the data and Fig. 18 compares the material removal rates.

Table 4 and Fig. 17 validate that the dimensions of the crater, as predicted by SPH, align well with the experimental data for the three scenarios. The largest discrepancy seen is 13.8% and 22% in the radius and depth, respectively. However, the magnitude of this inaccuracy is significantly lesser compared to the errors documented in the FEA findings published in the literature.

The material removal rate shown in Fig. 18 confirms that the SPH model predicts the results with less than 11% error compared to experiments in case 2, while the error drops to less than 6% in the other cases (see Table 5 for process parameters). The error range is rather small given the intricate nature of the EDM process and the several factors that affect the process, such as flushing efficiency dependency on the discharge energy, the temperature-dependent thermal properties, and the condition of the workpiece surface etc.

To ensure an exhaustive validation, the simulations were run for another 9 different combination of process

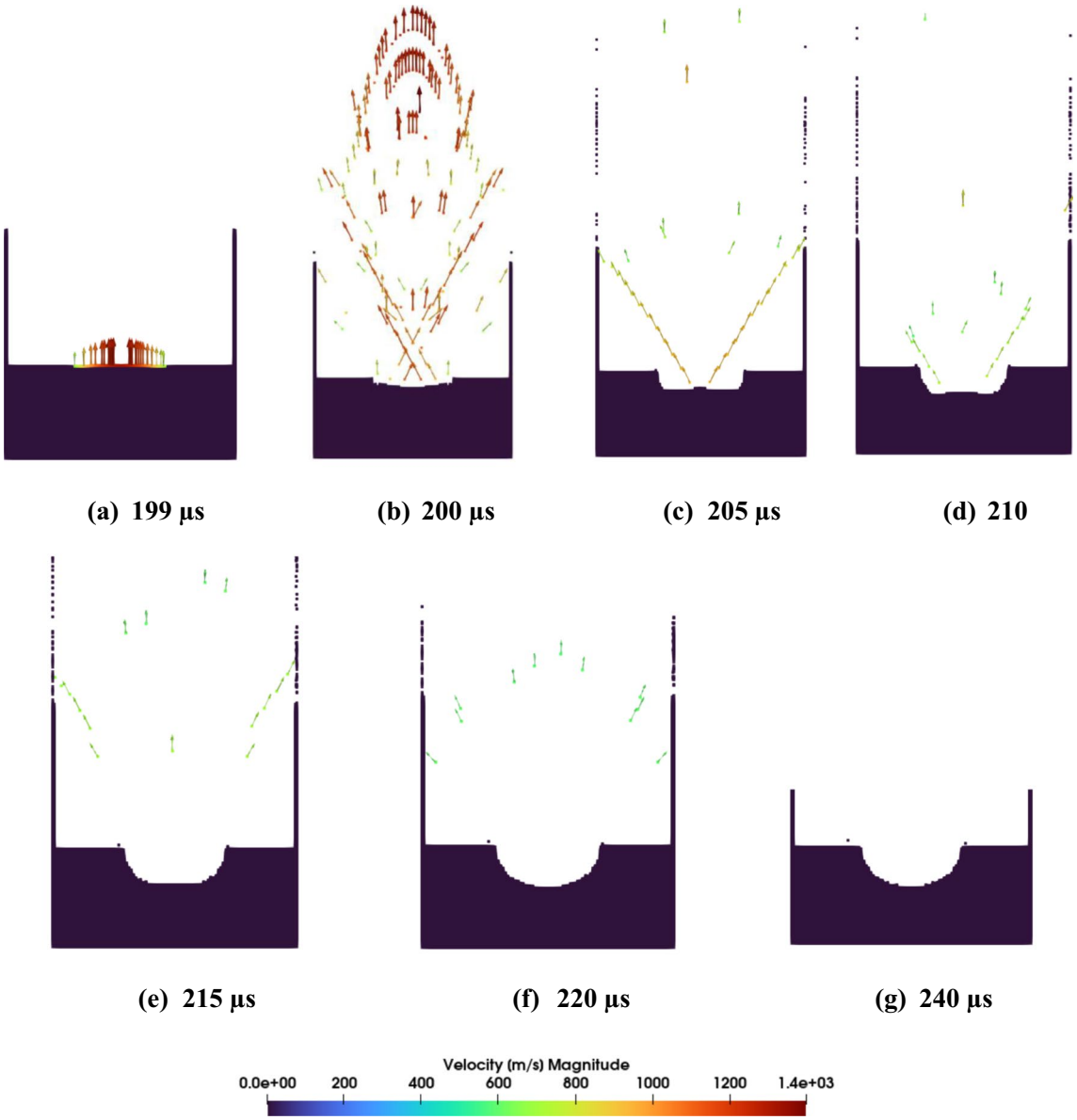

Fig. 15 Machined material velocity field and the crater formed using 60 A and 200 µs spark

parameters including pulse-ON-time, pulse-OFF-time, voltage and current. The results are also compared an analytical solution model developed by the same researchers. Figure 19 shows the calculated and measured MRR for the nine processing cases and it is evident that SPH calculations were the closest to the experimental results either at small (0.32 mJ) or high discharge energy (62.5 mJ) while FEA and analytical models significantly and consistently over-predicted the MRR. The error value in MRR using SPH ranges between 2 and 12% and increases gradually with the discharge energy. However, out of the 9 cases, only two scenarios (cases 2 and 8) generated larger errors up to 31%; however, it is difficult to determine whether those values are out of the limits because Assarzadeh and Ghoreishi [39] did not provide error bars for their experimental data. Despite that, th eSPH model still maintained a very good correlation with experiments compared to the other data.

The increase in the error may be expected to be larger at higher energy levels due to the increase in the crater's dimensions and the area of the workpiece exposed to the plasma, which may include more defects than the small areas. Furthermore, the flushing efficiency of the process also drops at higher discharge energy, and hence the actual EDM rate would be slightly smaller than that in the

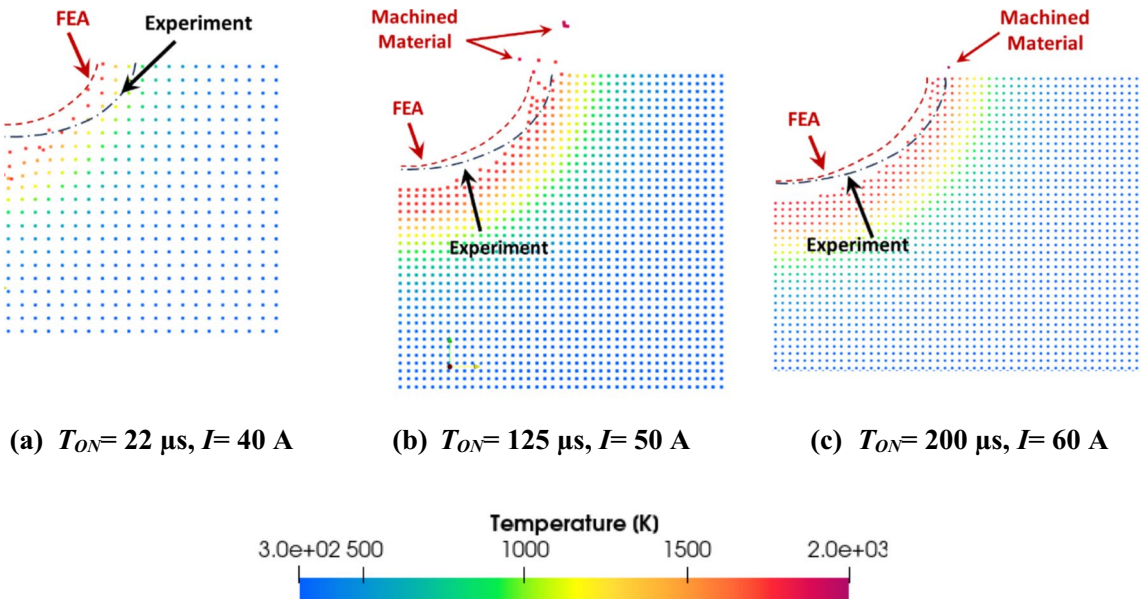

Fig. 16 Crater profile comparison between our SPH model and experiments by Assarzadeh and Ghoreishi [39] and FEA by Jithin et al. [47]

Table 4 Crater radius and depth comparison at three different cases, all dimensions are in microns

Case	Variables		Exp [39]		FEA [47]		FEA [39]		SPH	
	Current (A)	Time-ON (µs)	Rad	Dep	Rad	Dep	Rad	Dep	Rad	Dep
1	40	22	47.6	27.6	33.5	22.5	39	31.5	41	32.8
2	50	125	94.2	58.4	81	56.5	83.5	64.5	93.70	71.3
3	60	200	116.3	70.8	103.5	69.5	105.5	79	110.4	79.5

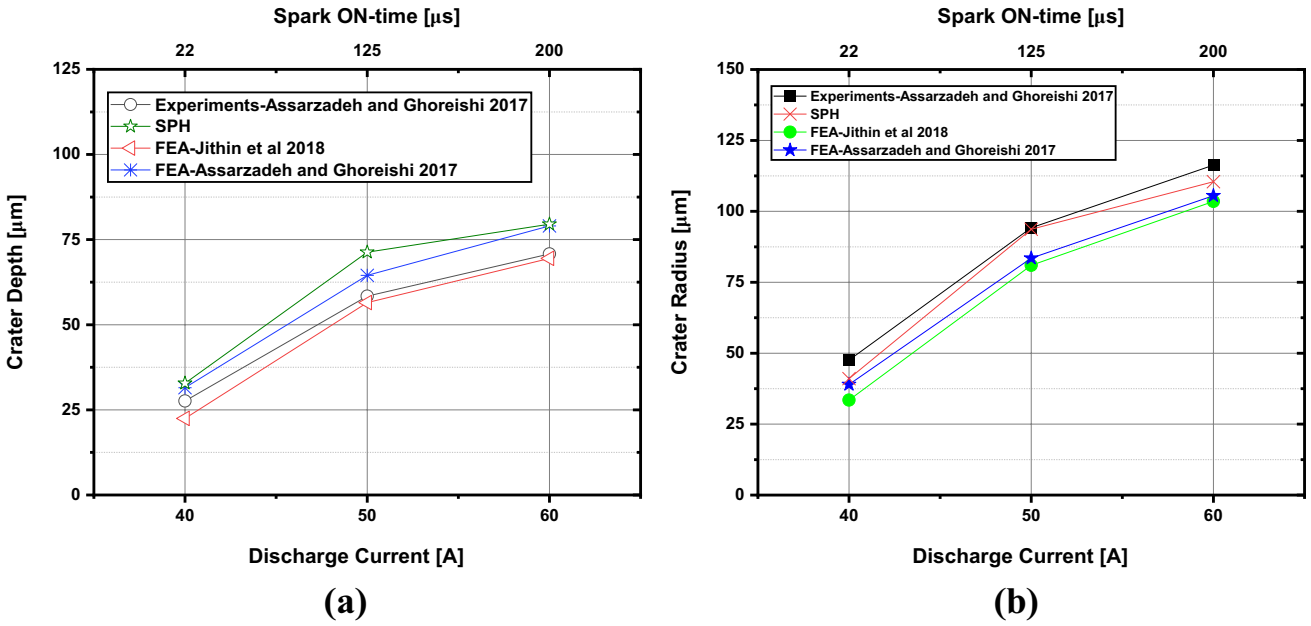

Fig. 17 Effect of process parameters on crater **a** depth and **b** radius compared to experiments and FEA models [39, 47]

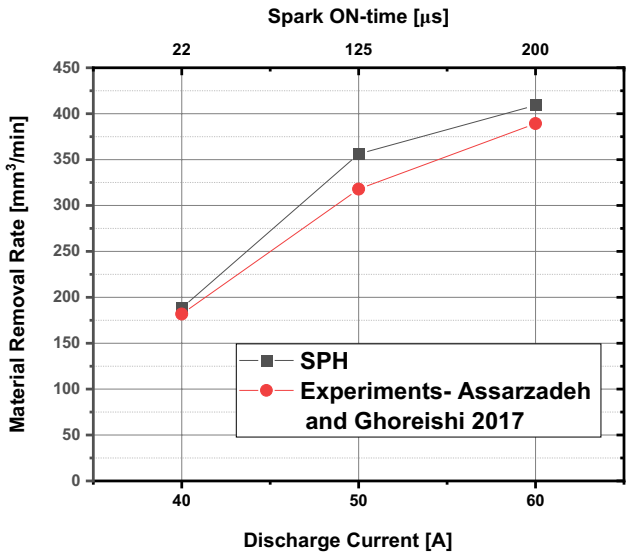

Fig. 18 Material removal rate comparison between SPH predictions and experiments

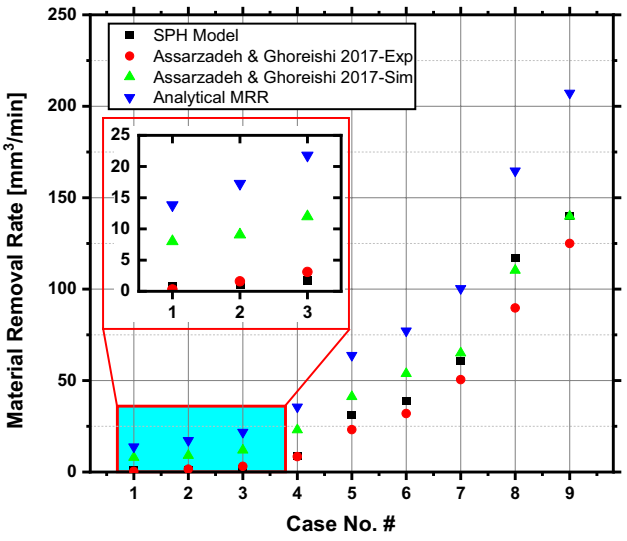

Fig. 19 MRR (mm^3/min) for EDM of AISI 304 Steel using a constant discharge voltage of 25 V

simulation, which neglects the defects or irregularities on the workpiece surface. This will be improved in future simulations where surface condition and topography can be considered.

To extend the validation, the SPH model was also tested for machining one of the most common difficult-to-machine Inconel 718 alloy. Kliuev et al. developed a model to predict the crater's profile using plasma channel radius calculations based on constant values fitted from the experiment results, as shown in Table 6. The plasma channel radius equation is taken as follows [45];

$$r_s = V_p \cdot t_{ON}^{0.2} + r_0 \tag{15}$$

where V_p is a constant, and r_0 is the initial radius.

Although this approach makes it almost impossible to use this model without experimentation, the provided cases were used to test the SPH model's accuracy.

It is clear from Fig. 20 that the SPH model provided a very good correlation with the experimental results and the dimensions mostly lay within the values of the error ranges. Both models' predictions were also close despite the slight drop in the SPH predictions of the crater radii. The difference can be due to the fact that Kliuev et al. neglected the material's vapourisation and relied on eroding only the molten material. This of course undermines the real scenario in which the vaporised material takes some of the heat away from the machined area and is affected by the flushing efficiency of the process, which was assumed 100% in this model.

Table 5 Material removal rate (mm^3/min) for EDM of Stainless Steel SS304 using a constant discharge voltage of 25 V, compared to data from [39]

Sample	T_on (µs)	T_off (µs)	Current (A)	SPH	Ref-Exp	Ref-Sim	Analytical
Case 1	5.6	1.0	2.34	0.8	0.3	8.0	13.8
Case 2	7.5	1.3	2.83	1.1	1.6	9.1	17.3
Case 3	13.0	2.4	3.67	1.7	3.1	12.0	21.8
Case 4	18.0	2.4	5.3	8.6	8.4	23.0	35.6
Case 5	24.0	2.4	8.5	31.2	23.2	41.2	63.8
Case 6	32.0	2.4	10	38.9	32	53.8	77.2
Case 7	42.0	3.2	12.8	60.7	50.5	65.1	100.3
Case 8	56.0	3.2	20	116.8	89.7	110.3	164.7
Case 9	100.0	4.2	25	140.0	125	139.8	207.2

Table 6 EDM process parameters for machining Inconel 718 as per Kliuev et al. [45]

Sample	T_on (µs)	Current (A)	Voltage (V)	F_a	Constant V_p (m/s)	Initial radius (µm)
Case 1	40	30	200	0.15764	36.343	100
Case 2	20	30	150	0.19600	57.856	100
Case 3	30	20	150	0.15676	50	100
Case 4	20	10	100	0.21713	38.729	87

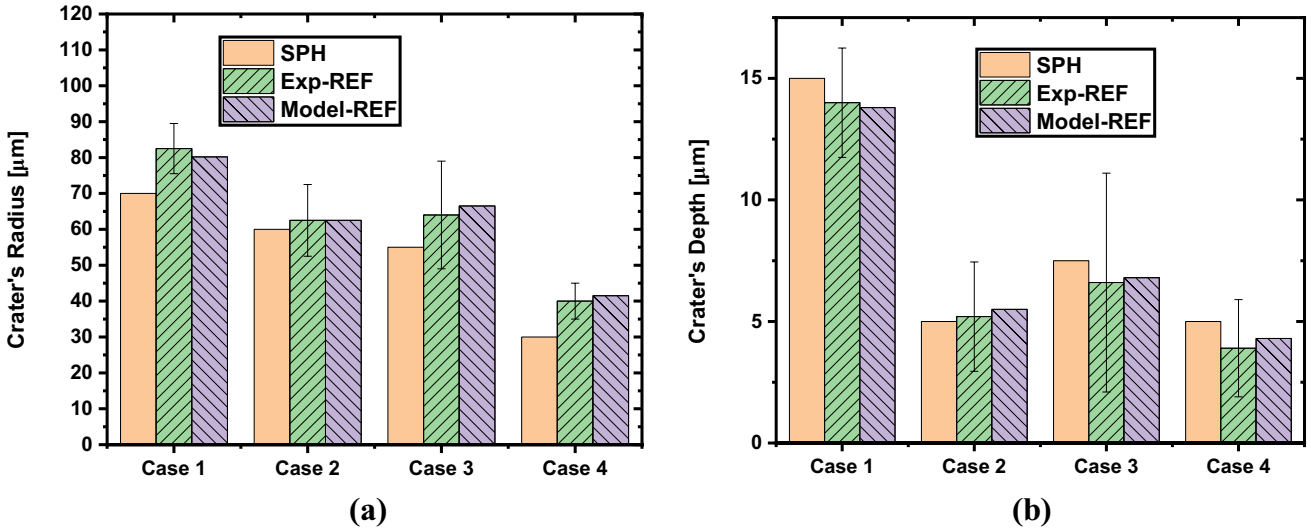

Fig. 20 Effect of process parameters on crater **a** radius and **b** depth compared to experiments and FEA models [45]

5 Conclusions

Our Smoothed Particle Hydrodynamics model was able to capture, for the first time, the machined materials during EDM of two workpiece materials, using a range of process parameters and two types of generation circuits. The main conclusions that can be drawn from this work are as follows:

- The SPH model successfully simulated the machined material of Ti–6AL–4V and AISI 304 Steel, considering their temperature-dependent thermophysical properties, latent heat, a Gaussian heat source, a time-dependent plasma channel radius and two different heat sources.
- The SPH model was able to precisely capture the crater's profile and consistently predicted the MRR using a range of process parameters with an error of less than 2–22%, depending on the process parameters and workpiece material.
- The SPH predictions were closer to the experiments at lower discharge energy levels (0.32 mJ) at a 2% error, while the error increased to 22% at higher energy levels (62.5 mJ), yet SPH achieved more precise results compared to FEA and analytical solutions.
- The machined material's trajectories, velocity, temperature, and location were captured every 1 µs due to the lagrangian nature of the SPH method.

SPH model in this article enables researchers to properly understand the EDM process by visualising the machined material removal and to predict their trajectory, velocity field to understand their effect on the electrode wear and the dielectric flushing efficiency and hence optimise the process and inform practice.

Author contribution statement Ahmad W Alshaer: conceptualisation, methodology, validation, writing—original draft. Ramy Abdullah: validation, formal analysis, writing—review and editing. Fatema Rajab: validation, writing—review and editing. Azeez Barzanji: writing—review and editing. Omonigho Otanocha: writing—review and editing.

Data availability The data that has been used is confidential.

Declarations

Declaration of generative AI and AI-assisted technologies in the writing process During the preparation of this work, the author(s) used

QuillBot for grammar check and sentence structure improvement. After using this tool/service, the author(s) reviewed and edited the content as needed and take(s) full responsibility for the content of the publication.

Competing interests The authors have no relevant financial or non-financial interests to disclose.

References

1. Fattahi S, Ullah AMMS (2022) Optimization of dry electrical discharge machining of stainless steel using big data analytics. Procedia CIRP 112:316–321
2. Sen R, Paul S, Choudhuri B (2022) Investigation on wire electrical discharge machining of AISI 304 stainless steel. Mater Today: Proc 62:1210–1214
3. Dewangan S, Sukhwal G, Naidu S, Maheshwari L, Surana H, Kulkarni AR (2024) Optimization of input parameters used for machining heat-treated 0.2%-C steel under the EDM method. J Inst Eng (India): Ser D. https://doi.org/10.1007/s40033-024-00661-4
4. Paswan K, Pramanik A, Chattopadhyaya S, Sharma S, Singh G, Khan AM, Singh S (2023) An analysis of machining response parameters, crystalline structures, and surface topography during EDM of die-steel using EDM oil and liquid-based viscous dielectrics: a comparative analysis of machining performance. Arab J Sci Eng 48:11941–11957
5. Mahapatra KK, Biswal S, Tripathy S, Thatoi DN, Satapathy P (2023) Optimization of EDM process parameters in machining of titanium alloy used for aerospace applications. In: Tripathy S, Samantaray S, Ramkumar J, Mahapatra SS (eds) Recent advances in mechanical engineering. Springer Nature, Singapore, pp 163–172
6. Klocke F, Mohammadnejad M, Holsten M, Ehle L, Zeis M, Klink A (2018) A comparative study of polarity-related effects in single discharge EDM of titanium and iron alloys. Procedia CIRP 68:52–57
7. Akincioglu S (2022) Taguchi Optimization of multiple performance characteristics in the electrical discharge machining of the TIGR2. Facta Univ Ser: Mech Eng 20:237–253
8. Chen Y, Li C, Li S, Xu M, Huang L, Li S, Li P, Qiu X, Ko TJ (2023) Study on the formation of the crater and modified layer in EDM titanium alloys based on fluid–solid coupled temperature field model. Int J Precis Eng Manuf 24:337–351
9. Papazoglou EL, Karmiris-Obratański P, Leszczyńska-Madej B, Markopoulos AP (2021) A study on electrical discharge machining of titanium Grade2 with experimental and theoretical analysis. Sci Rep 11:8971
10. Kar SK, Mishra PK, Sahu AK, Mahapatra SS, Thomas J (2023) Multi-objective optimization of wire-EDM of Inconel 625 by using desirability function approach. Int J Interact Des Manuf (IJIDeM) 17:931–938
11. Ye L, Saxena KK, Huang S, Qian J, Vleugels J, Reynaerts D (2022) Experimental investigations on micro-EDM milling of niobium carbide-nickel based cermet using statistical and empirical techniques. Procedia CIRP 113:47–52
12. Paswan K, Sharma S, Dwivedi SP, Abdulameer MK, Li C, Yasin Y, Abbas M, Tag-Eldin EM (2023) An analysis of microstructural morphology, surface topography, surface integrity, recast layer, and machining performance of graphene nanosheets on Inconel 718 superalloy: Investigating the impact on EDM characteristics, surface characterizations, and optimization. J Market Res 27:7138–7158
13. Narayana Reddy B, Venkata Ramana R, Jameel Basha SM, Bhargava Ramu T (2023) Studies on effect of wire EDM process parameters on machining characteristics of Inconel 825 plate. Mater Today: Proceedings, In press. https://doi.org/10.1016/j.matpr.2023.04.469
14. Arif U, Khan IA, Hasan F (2023) Thermal modeling and parametric optimization for machining of aluminum (Al-10%SiCmicro-SiCnano)-based hybrid composite using spark erosion. J Mater Eng Perf, 1544–1024. https://doi.org/10.1007/s11665-023-09042-6
15. Pain P, Bose GK, Bose D (2023) Parametric analysis and optimization of aluminium and SS 204 material using micro-EDM system. Int J Interact Des Manuf (IJIDeM) 17:3025–3042
16. Rajmohan K, Vivekanandhan M, Senthilkumar C (2024) Modelling and parametric optimization of EDM of Al 8081/SiCp composite through DEAR approach. Int J Interact Des Manuf (IJIDeM) 18:697–708
17. Schumacher BM (2004) After 60 years of EDM the discharge process remains still disputed. J Mater Process Technol 149:376–381
18. Papazoglou EL, Karmiris-Obratański P, Karkalos NE, Thangaraj M, Markopoulos AP (2023) Theoretical and experimental analysis of plasma radius expansion model in EDM: a comprehensive study. Int J Adv Manuf Technol 126:2429–2444
19. Raza S, Kishore H, Nirala CK, Rajurkar KP (2023) Multiphysics modelling and high-speed imaging-based validation of discharge plasma in micro-EDM. CIRP J Manuf Sci Technol 43:15–29
20. Yue X, Yang X (2020) Molecular dynamics simulation of material removal process and mechanism of EDM using a two-temperature model. Appl Surf Sci 528:147009
21. Yang X, Guo J, Chen X, Kunieda M (2011) Molecular dynamics simulation of the material removal mechanism in micro-EDM. Precis Eng 35:51–57
22. Weingärtner E, Kuster F, Wegener K (2012) Modeling and simulation of electrical discharge machining. Procedia CIRP 2:74–78
23. Somashekhar KP, Panda S, Mathew J, Ramachandran N (2015) Numerical simulation of micro-EDM model with multi-spark. Int J Adv Manuf Technol 76:83–90
24. Murali MS, Yeo S-H (2005) Process simulation and residual stress estimation of micro-electrodischarge machining using finite element method. Jpn J Appl Phys 44:5254
25. Qian J, Yang F, Wang J, Lauwers B, Reynaerts D (2015) Material removal mechanism in low-energy micro-EDM process. CIRP Ann 64:225–228
26. Cao P, Tong H, Li Y, Chen J (2023) Interelectrode gas–liquid-solid three-phase flow analysis and simulation for drilling holes with high aspect ratio by micro-EDM. Int J Adv Manuf Technol 128:5261–5276
27. Izquierdo B, Sánchez JA, Plaza S, Pombo I, Ortega N (2009) A numerical model of the EDM process considering the effect of multiple discharges. Int J Mach Tools Manuf 49:220–229
28. Jithin S, Bhandarkar UV, Joshi SS (2020) Multi-spark model for predicting surface roughness of electrical discharge textured surfaces. Int J Adv Manuf Technol 106:3741–3758
29. Yeo SH, Kurnia W, Tan PC (2008) Critical assessment and numerical comparison of electro-thermal models in EDM. J Mater Process Technol 203:241–251
30. Snoeys R, Dijck FSV (1971) Investigation of electro discharge machining operations by means of thermo-mathematical model. CIRP Ann 20:35–37

31. Dijck FSv, Dutré WL (1974) Heat conduction model for the calculation of the volume of molten metal in electric discharges. J Phys D: Appl Phys 7:899
32. Beck JV (1981) Transient temperatures in a semi-infinite cylinder heated by a disk heat source. Int J Heat Mass Transf 24:1631–1640
33. Beck JV (1981) Large time solutions for temperatures in a semi-infinite body with a disk heat source. Int J Heat Mass Transf 24:155–164
34. Pandey PC, Jilani ST (1986) Plasma channel growth and the resolidified layer in edm. Precis Eng 8:104–110
35. Tariq Jilani S, Pandey PC (1982) Analysis and modelling of edm parameters. Precis Eng 4:215–221
36. Tariq Jilani S, Pandey PC (1983) An analysis of surface erosion in electrical discharge machining. Wear 84:275–284
37. DiBitonto DD, Eubank PT, Patel MR, Barrufet MA (1989) Theoretical models of the electrical discharge machining process. I. A simple cathode erosion model. J Appl Phys 66:4095–4103
38. Bhaumik M, Maity K (2021) Finite element simulation and experimental investigation of Ti-5Al-2.5Sn titanium alloy during EDM process. Mater Today: Proc 46:24–29
39. Assarzadeh S, Ghoreishi M (2017) Electro-thermal-based finite element simulation and experimental validation of material removal in static gap single-spark die-sinking electro-discharge machining process. Proc Inst Mech Eng B: J Eng Manuf 231:28–47
40. Kalajahi HM, Ahmadi RS, Bavil Oliaei NS (2013) Experimental and finite element analysis of EDM process and investigation of material removal rate by response surface methodology. Int J Adv Manuf Technol 69:687–704
41. Gholipoor A, Shabgard MR, Mohammadpourfard M (2020) A novel approach to plasma channel radius determination and numerical modeling of electrical discharge machining process. J Braz Soc Mech Sci Eng 42:185
42. Tang J, Li Z, Yue X (2024) Numerical analysis of plasma channel characteristics and dynamic effects on molten pool in electrical discharge machining. Precis Eng 86:305–316
43. Li Q, Yang X (2023) Thermo-hydraulic analysis of melt pool dynamics and material removal on anode in electrical discharge machining. Int J Heat Mass Transf 203:123816
44. Padhi BN, Choudhury SK, Janakarajan R (2023) Thermal modeling and experimentation on discharge energy distribution and plasma flushing for a single discharge in EDM of D2 steel. Proc Inst Mech Eng E: J Process Mech Eng 0(0). https://doi.org/10.1177/09544089231194872
45. Kliuev M, Florio K, Akbari M, Wegener K (2019) Influence of energy fraction in EDM drilling of Inconel 718 by statistical analysis and finite element crater-modelling. J Manuf Process 40:84–93
46. Alshaer AW, Rogers BD, Li L (2017) Smoothed Particle Hydrodynamics (SPH) modelling of transient heat transfer in pulsed laser ablation of Al and associated free-surface problems. Comput Mater Sci 127:161–179
47. Jithin S, Raut A, Bhandarkar UV, Joshi SS (2018) FE modeling for single spark in EDM considering plasma flushing efficiency. In: 46th SME North American Manufacturing Research Conference, Procedia Manufacturing, NAMRC 46, Texas, USA. pp 617–628
48. Perez R, Rojas H, Walder G, Flükiger R (2004) Theoretical modeling of energy balance in electroerosion. J Mater Process Technol 149:198–203
49. Motoki M, Hashiguchi K (1967) Energy distribution at the gap in electric discharge machining. CIRP Ann: Manuf Technol XIV:485–489
50. Konig W, Wertheim R, Zvirin Y, Toren M, (1975) Material removal and energy distribution in electric discharge machining. CIRP Ann: Manuf Technol 95–100 STC
51. Jithin S, Bhandarkar UV, Joshi SS (2017) Analytical simulation of random textures generated in electrical discharge texturing. J Manuf Sci Eng 139:111002
52. Patel MR, Barrufet MA, Eubank PT, DiBitonto DD (1989) Theoretical models of the electrical discharge machining process. II. The anode erosion model. J Appl Phys 66:4104–4111
53. Atkins PW, De Paula J (2002) Atkins' physical chemistry. Oxford University Press, Oxford
54. Kelly R (1990) On the dual role of the Knudsen layer and unsteady, adiabatic expansion in pulse sputtering phenomena. J Chem Phys 92:5047–5056
55. Alshaer AW, Rogers BD, Li L (2016) Smoothed particle hydrodynamics modelling of pulsed laser ablation of aluminium and associated free-surface problems. In: 11th International SPHERIC (SPHERIC 2016) Workshop, Technische Universität München (TUM) in Garching Germany
56. Liu GR, Liu MB (2003) Smoothed particle hydrodynamics: a meshfree particle method. World Scientific, New Jersey
57. Morris JP, Fox PJ, Zhu Y (1997) Modeling Low Reynolds number incompressible flows using SPH. J Comput Phys 136:214–226
58. Yue X, Yang X (2021) The role of discharge plasma on molten pool dynamics in EDM. J Mater Process Technol 293:117092
59. Singh M, Sharma S, Ramkumar J (2020) Numerical simulation of melt-pool hydrodynamics in μ-EDM process. Procedia CIRP 95:226–231